Applied Catalysis B: Environmental 219 (2017) 132–141

Contents lists available at ScienceDirect

Applied Catalysis B: Environmental

journal homepage: www.elsevier.com/locate/apcatb

A sillenite-type $Bi_{12}MnO_{20}$ photocatalyst: UV, visible and infrared lights responsive photocatalytic properties induced by the hybridization of Mn 3d and O 2p orbitals

Xiaoyong Wu[a,1], Mingmeng Li[a,1], Jun Li[a], Gaoke Zhang[a,*], Shu Yin[b]

[a] Hubei Key Laboratory of Mineral Resources Processing and Environment, Hubei Provincial Collaborative Innovation Center for High Efficient Utilization of Vanadium Resources, School of Resources and Environmental Engineering, Wuhan University of Technology, 122 Luoshi Road, Wuhan 430070, China
[b] Institute of Multidisciplinary Research for Advanced Materials, Tohoku University, Sendai 9808578, Japan

ARTICLE INFO

Article history:
Received 9 February 2017
Received in revised form 18 June 2017
Accepted 10 July 2017
Available online 11 July 2017

Keywords:
Sillenite structure
$Bi_{12}MnO_{20}$
Full spectrum
Photocatalytic reduction
Mn^{4+} incorporation

ABSTRACT

Although UV and visible lights induced photocatalysis has been well developed in recent years, the full spectrum of UV, visible and NIR lights responsive photocatalysis is still few, which is beneficial for energy utilization and practical application. Herein, we report a new sillenite-type $Bi_{12}MnO_{20}$ photocatalyst prepared by a facile sol-gel method. Through incorporating the Mn^{4+} ions into tetrahedral sites of metastable cubic γ-Bi_2O_3 to split the 3d orbits of Mn^{4+}, the new-produced $Bi_{12}MnO_{20}$ crystal presents peculiar and strong absorption capability, covering the full spectrum of UV, visible and NIR lights in the range of 200–1300 nm. The DFT calculation further confirms the existence of intermediate band state in the band gap of $Bi_{12}MnO_{20}$, which was formed by the hybrid of O 2p and Mn 3d orbits. More importantly, under the irradiation of UV, visible and NIR lights, $Bi_{12}MnO_{20}$ product exhibits excellent photocatalytic reduction activity for Cr(VI), which is mainly due to the relatively good charge separation enhanced by unique electronic structure of the Bi^{3+} $6s^2$ lone pair, the suitable band positions and the introduction of intermediate band state. In addition, the $Bi_{12}MnO_{20}$ specimen also displays good visible light driven photocatalytic oxidation property for acid red G, which is mainly caused by h^+ and $^{\bullet}O_2^-$ species. The as-prepared $Bi_{12}MnO_{20}$ semiconductor would provide a new potential to fulfill the full spectrum responsive photocatalysis.
© 2017 Elsevier B.V. All rights reserved.

1. Introduction

With the rapid development of metallurgical and chemical industries, a growing number of heavy metal contaminants have been released into natural water [1–4]. Typically, chromium (VI) has been widely regarded as one of the most harmful heavy metal contaminants originated from leather tanning, textile manufacturing, fertilizing, petroleum refining, etc [5–8]. It is very harmful to most organisms, lung, kidney and nasal septum owing to its easy migration and carcinogenicity. On the contrast, the reduced chromium (III) is much less toxic or no and stable, which can easily be precipitated in alkaline and neutral aqueous solutions. And even it has been considered as healthy element and nutrition for human beings and many organisms [9–12]. Therefore, the reduction of chromium (VI) to chromium (III) would be a promising way to alleviate or solve the chromium (VI) contamination in natural water. In this case, many efforts have been made to remediate chromium (VI) pollution such as chemical precipitation, microorganisms, electrodialysis, etc [13–15]. Among them, photocatalysis as a green chemical technology has drawn peculiar attention over other methods due to its relatively high efficiency, low cost and environmental friendly [16,17]. Many UV and visible light responsive photocatalysts such as TiO_2, ZnO, SnS_2, C_3N_4, etc [18–25]. were correspondingly developed to decontamination of chromium (VI) to chromium (III) in aqueous solution, while the near infrared light (NIR) induced one is still very few [26]. It is well-known that the natural solar light is composed of ca. 5% UV light, 45% visible light and about 50% NIR [27]. Thus, proposing full spectrum of UV, visible and NIR driven photocatalyst for chromium (VI) reduction is fascinating and still strongly required [28–32].

As is well known, Bi based compounds (e.g. BiOCl, Bi_2WO_6, Bi_2MoO_6, $NaBiO_3$, $BiVO_4$ and Bi_2O_3, etc.) have become hotspot as potential photocatalysts, owing to their unique d10 configuration and $6s^2$ lone pair of Bi^{3+} ions in the lattice of crystal. These typical electronic structures facilitate the separation of photogenerated

* Corresponding author.
E-mail address: gkzhang@whut.edu.cn (G. Zhang).
[1] Xiaoyong Wu and Mingmeng Li have made equal contribution to this paper.

http://dx.doi.org/10.1016/j.apcatb.2017.07.025
0926-3373/© 2017 Elsevier B.V. All rights reserved.

electron-hole pairs and the narrowing of band gap for semiconductor by the contribution of orbital hybridization with other ions [33–38]. Recently, the family of sillenites with the general formula of $Bi_{12}MO_{20}$ (M = Ti, Ge, Si, etc.), as a new series of Bi based compounds, have also been paid increasing attention for photocatalysis because of their peculiar electronic structure and M incorporation in the MO_4 tetrahedra [39–41]. For instance, Yao, et al. [39] reported the photocatalytic property of $Bi_{12}TiO_{20}$ crystals, finding that the methyl orange solution could be quickly photodegraded during 1.5 h under the visible light irradiation. Zhang groups [40] controllably synthesized visible light responsive $Bi_{12}GeO_{20}$ by hydrothermal method for the degradation of RhB. However, all of them can only be excited by UV and visible light, while NIR light induced one is not feasible for photo-decontamination due to their wide band gap. On the other hand, the transition metal Mn is well-acknowledged as one of dopant stars in photocatalysis semiconductor to narrow band gap and improve the separation of charge carriers, owing to its unique 3d electronic structure. Particularly, when it is doped into some of suitable semiconductor crystals, the 3d orbits of Mn ions can be easily split to two e_g and three t_{2g} orbits, which will enter into band gap, or hybrid with oxygen [42–44]. In this case, the light absorption capability of compound can be extended to long wavelength of visible light or even NIR light. So if Mn^{4+} ion was incorporated into metastable cubic γ-Bi_2O_3 to form sillenite $Bi_{12}MnO_{20}$, the unique MnO_4 tetrahedra unit in $Bi_{12}MnO_{20}$ is possible to induce full spectrum active photocatalysis in the whole UV, visible and NIR lights range. To the best of our knowledge, there is no research about the photocatalysis of $Bi_{12}MnO_{20}$ up to now, except for the magnetic property, let alone the full spectrum of UV, visible and NIR lights induced photocatalysis for $Bi_{12}MnO_{20}$.

In this work, Mn^{4+} ions have been successfully incorporated into metastable cubic γ-Bi_2O_3 to form sillenite $Bi_{12}MnO_{20}$ compound by a facile sol-gel method, expecting to fulfill the full spectrum active photocatalyst. The effects of calcination temperature and time on the formation of sillenite $Bi_{12}MnO_{20}$ were conducted. Meanwhile, the DFT calculation was employed to study the band structure of the sample. In addition, the photocatalytic activity of $Bi_{12}MnO_{20}$ was examined by photocatalytic reduction of chromium (VI) under the irradiation of UV, visible and NIR lights, and also photocatalytic oxidation of acid red G (ARG) under visible light. The influences of working pH values, calcination temperature and time, active species and photocatalytic stability on the photocatalytic properties of $Bi_{12}MnO_{20}$ were further investigated. Finally, the possible photocatalytic degradation mechanism of $Bi_{12}MnO_{20}$ under UV, visible and NIR lights driven was also investigated.

2. Experimental

2.1. Sample preparation

$Bi_{12}MnO_{20}$ (BMO) particles were prepared by a facile sol-gel method. All chemical are of analytical purity and were used directly without any treatment.

In a typical procedure, 0.072 mol citric acid monohydrate and 0.018 mol $Bi(NO_3)_3{\cdot}5H_2O$ were added into 30 mL distilled water with continuously magnetic stirring. Besides, 14 g EDTA was completely dissolved in 20 mL of ammonia under vigorous stirring, which was then transferred into the above-prepared water solution in thermostatic water-bath (80 °C) with fiercely stirring until the solution was changed to the transparent, named solution A. Before the formation of white sticky sol, 1.5 mmol $C_4H_6MnO_4{\cdot}4H_2O$ was dissolved in 50 mL of ammonia under vigorous stirring and then transferred into solution A under thermostatic water-bath (80 °C) stirring. After that, the prepared sol was moved into ceramic crucible, which was heated in an electric furnace until the sol was carbonized to black bituminous material. Then, the black bituminous material was further scorched 2 h at 400 °C to remove organic substances on gel, followed by cooling down to the room temperature and grinding. Finally, the powders were calcined again at various temperatures for different time. The prepared samples $Bi_{12}MnO_{20}$ were designated as BMO-T-H. The T indicates the calcined temperature and H implies the calcined time.

2.2. Characterization

The crystal structure of the $Bi_{12}MnO_{20}$ powders was checked by powder X-ray diffraction (XRD) analysis (D/MAX-RB diffractometer) with Cu_{Ka} radiation. The atom state and valence position of elements in $Bi_{12}MnO_{20}$ sample were characterized by X-ray photoelectron spectroscopy (XPS, VG Multilab2000). The binding energy in the XPS analysis was calibrated by 284.6 eV of C 1s as reference. UV photoelectron spectroscopy (UPS, AXIS-ULTRA DLD-600W) test was used to determine the position of valence band using He I gas (21.22 eV) as a UV source. The morphology, particle size and structure of the products were carried out by scanning electron microscopy (SEM, JSM-5610LV), transmission electron microscopy (JEOL-2010 TEM), high-resolution transmission electron microscopy (HRTEM) and selected area electron diffraction (SAED). The optical absorption property of samples was tested by a UV–vis-NIR spectrophotometer (Lambda 750S). The photoluminescence property of product was evaluated by fluorescence spectrophotometer (RF-5301 PC). The specific surface area of samples were measured by a multipoint Brunauer–Emmett–Teller (BET) method.

2.3. Photocatalytic activity test

The photocatalytic activities of the samples were evaluated by degrading $K_2Cr_2O_7$ solution (Cr (VI)) under the irradiation of UV, visible and NIR lights, adopting 20 W (0.75 mW Cm^{-2}) 254 nm UV lamp, 300 W (100 mW Cm^{-2}) Dy lamp with 400 nm cutoff filter and 100 W (31.3 mW Cm^{-2}) NIR LED (peaked at ca. 815 nm) as light sources, respectively, and decontaminating ARG aqueous solution under visible light irradiation, using 400 nm cutoff filter coupled 300 W Dy lamp as light source. For the degradation of Cr (VI), certain amounts of photocatalyst (1 g/L, 2 g/L and 3 g/L) were dispersed into 100 mL of $K_2Cr_2O_7$ solution (10 mg/L, 20 mg/L, 30 mg/L). Before illumination, the suspension was magnetically stirred for 30 min in the dark to keep adsorption-desorption balance of Cr (VI). After that, the Cr (VI) solution was irradiated by different light sources for 2 h. At a defined time interval, 7 mL of suspension was sampled and centrifuged to get rid of the sample particles. Then, 0.5 mL of sulfuric acid solution (1:1), 0.5 mL of phosphoric acid solution (1:1) and 2 mL of color developing agent were added to the 5 mL of above supernatant, shaking well and waiting for 5–10 min. Finally, the residue concentration of Cr (VI) was measured at the wavelength of 540 nm via a UV–vis spectrophotometer (UV1100). For the degradation of ARG aqueous solution, 0.2 g of the sample was added to 100 mL of ARG aqueous solution (10 mg/L). Prior to illumination, the suspensions were stirred in the dark for 0.5 h to ensure the adsorption-desorption balance. Then, the Dy lamp was turned on to irradiate the ARG aqueous solution under magnetic stirring. At a defined time interval, 7 mL of suspension was sampled and centrifuged to get rid of the photocatalyst particles. Finally, the concentration of ARG aqueous solution was measured at wavelength of 505 nm by UV–vis spectrophotometer. All photocatalytic tests were kept at room temperature by cycling water system to eliminate the effect of thermal on the photocatalytic activity. In order to calculate apparent quantum efficiency (AQE) of sample, the visible LED

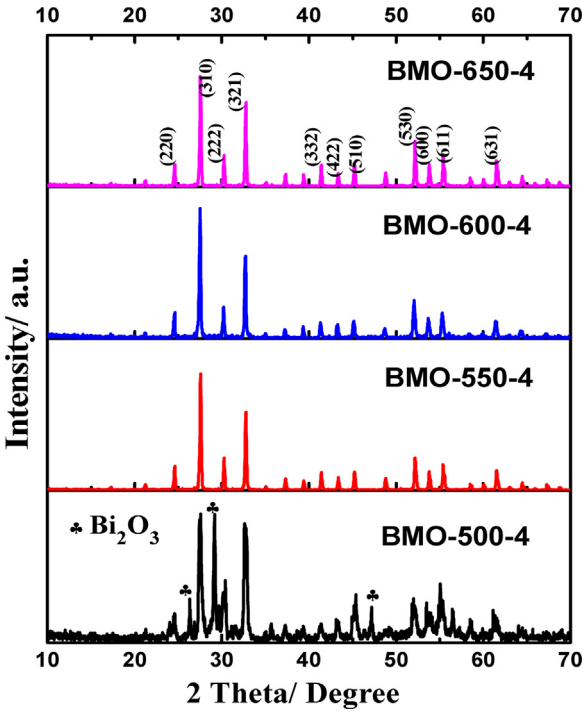

Fig. 1. XRD patterns of BMO prepared at various temperatures for 4 h.

(420 nm) (88.6 mW Cm^{-2}) was also solely employed to irradiate the sample for Cr (VI) photocatalytic reduction.

The radical species trapping experiments were also conducted to estimate the active species in photocatalytic degradation process. $Na_2C_2O_4$ (2 mM) and 1, 4-benzoquinone (BQ, 2 mM) were employed as the scavengers of h^+ and $^{\bullet}O_2^-$ to study the effect of active species on the photocatalytic property of samples, respectively.

2.4. Electronic structure calculations

The electronic structure calculation was conducted by the density functional theory (DFT) + U method with the Perdew-Burke-Ernzerhof (PBE) GGA functional encoded via the Vienna ab initio. To begin with, the geometry optimizations were performed to ensure the accurate of calculation. The energy cut-off was set to 400 eV, and the Brillouin zones of $Bi_{12}MnO_{20}$ were sampled in $9 \times 9 \times 9$ k-point grids. All of the geometry optimization was carried out as components of residual force were less than 0.02 eV/Å and the iterative energy difference was less than 10^{-4} eV. The U values of O 2p, Bi 6p and Mn 3d were set as 7.0, 7.0 and 6.0 eV, respectively. All the calculations were carried out at absolute zero temperature (0 K).

3. Results and discussion

Fig. 1 shows the XRD patterns of the BMO samples as a function of reaction temperatures. It is apparent that as the sample was heat-treated at 500 °C for 4 h, the main diffraction peaks of BMO-500-4 can be indexed to the JCPDS card No. 45-0276 of $Bi_{12}MnO_{20}$ with the space group I23 and a = 10.206, which corresponds to the typical sillenite type structure. However, there are still a few impurity peaks, belonging to Bi_2O_3, existed as symbolled in the figure. When the calcined temperature increased to 550 °C or above, the Bi_2O_3 impurity disappeared and all diffraction peaks are well accordance with the pure $Bi_{12}MnO_{20}$. This phenomenon indicates that the Bi_2O_3 was the intermediate product in the formation of $Bi_{12}MnO_{20}$ and the lowest temperature for the formation of pure $Bi_{12}MnO_{20}$ crystal was 550 °C. The influence of reaction time on the crystal formation of $Bi_{12}MnO_{20}$ with respect to various reaction temperatures were presented in Fig. 2. For the consideration of reaction time at 550 °C, some impurity peaks belonged to Bi_2O_3 were still existed at 2 and 3 h, and the pure $Bi_{12}MnO_{20}$ was produced until 4 h. While as the reaction temperature rose to 600 and 650 °C, all the samples exhibited the pure BMO one regardless of reaction time. So the optimal reaction condition for the formation of pure BMO crystal was fixed at 550 °C for 4 h.

Fig. 3 displays the morphology and details of crystal structure of the BMO-550-4 sample. In Fig. 3(a), it can be clearly seen that the morphology of BMO particle formed like as a peanut with the diameter of ca.1 μm. Furthermore, with the increment of annealing temperature from 550 to 650 °C as supplemented in the SEM images of Fig. S1, the BMO particle became more uniform and smoother, but derived increased particle size. As shown in Fig. 3(b), the regular lattice spacing of 0.275 nm is well consistent with the (3 2 1) crystal plane of BMO crystal (JCPDS no. 45-0276). Moreover, the SAED pattern in Fig. 3(c) illustrates a paralleled spot pattern, indicating that the prepared products possess the single crystal feature. Meanwhile, the reciprocal lattice of 3.633 nm^{-1} interval is nicely agreement with the (3 2 1) crystal plane of body-centered cubic BMO crystal and the reciprocal lattice of 5.549 nm^{-1} interval is assigned to the (440) crystal plane of body-centered cubic BMO crystal. The calculated angle between these two crystal planes is 18.23°, which is well indexed to the theoretical angle of 19.10°. So the above-discussed HRTEM and SAED can further confirm the formation of sillenite type $Bi_{12}MnO_{20}$ crystal by the sol-gel method.

In order to study the chemical state and surface composition of BMO sample, the XPS analysis was employed. Fig. 4 represents the survey, Bi 4f, Mn 2p and O 1 s spectra of BMO-550-4, BMO-600-4 and BMO-650-4 samples, and all samples presented the similar characteristic lines. To be concrete, in Fig. 4a, Bi, Mn and O all exhibited in the survey spectra of three samples and no impurity content appeared except for the adventitious carbon [40]. The Bi 4f XPS spectra in Fig. 4b showed two peaks at 158.5 and 163.8 eV which are attributed to the binding energies of Bi^{3+} for $4f_{7/2}$ and $4f_{5/2}$ core levels, respectively. As for Mn 2p XPS spectra in Fig. 4c, there are also two obvious peaks appeared at 642.2 and 653.4 eV, which are ascribed to the binding energies of Mn^{4+} for $2p_{3/2}$ and $2p_{1/2}$ core levels, separately. These indicate that the Mn ion existed in the BMO by the form of pure Mn^{4+} instead of other reduced valence values or mixed values [45]. In addition, the BMO-650-4 and BMO-600-4 samples exhibited similar area of these two peaks and little bit larger than BMO-550-4 sample, indicating probably more Mn^{4+} ions have been incorporated in BMO-650-4 and BMO-600-4 samples compared with that of BMO-550-4 sample. Fig. 4(d) apparently exhibits asymmetry shape O 1s XPS spectra. These spectra could be fitted into two Gaussian peaks located at 529.4 and 531.2 eV. The peak at 529.4 eV is corresponding to the binding energy of bridging oxygen atom from Bi-O-Bi bonds [46]. While the peak at 531.2 eV should be assigned to the binding energy of oxygen in the framework bond of Mn-O-Bi [47].

The optical properties of the BMO sample were investigated by UV–vis-NIR spectrophotometer and fluorescence spectrophotometer as shown in Fig. 5. Fig. 5 (a) shows the DRS of BMO samples calcined at different temperatures. Generally speaking, the semiconductor photocatalyst should exhibit only one main absorption peak in DRS owing to its intrinsic band gap [48,49]. However, in this work, it is noteworthy that all three samples present two main absorption peaks located at ca.480 and 780 nm, respectively. More importantly, these two strong absorption peaks covers the full spectrum of UV, visible and NIR lights from 200 to 1300 nm. The first absorption band from ca. 200–680 nm should be attributed to the charge transfer happened in the intrinsic band gap of $Bi_{12}MnO_{20}$

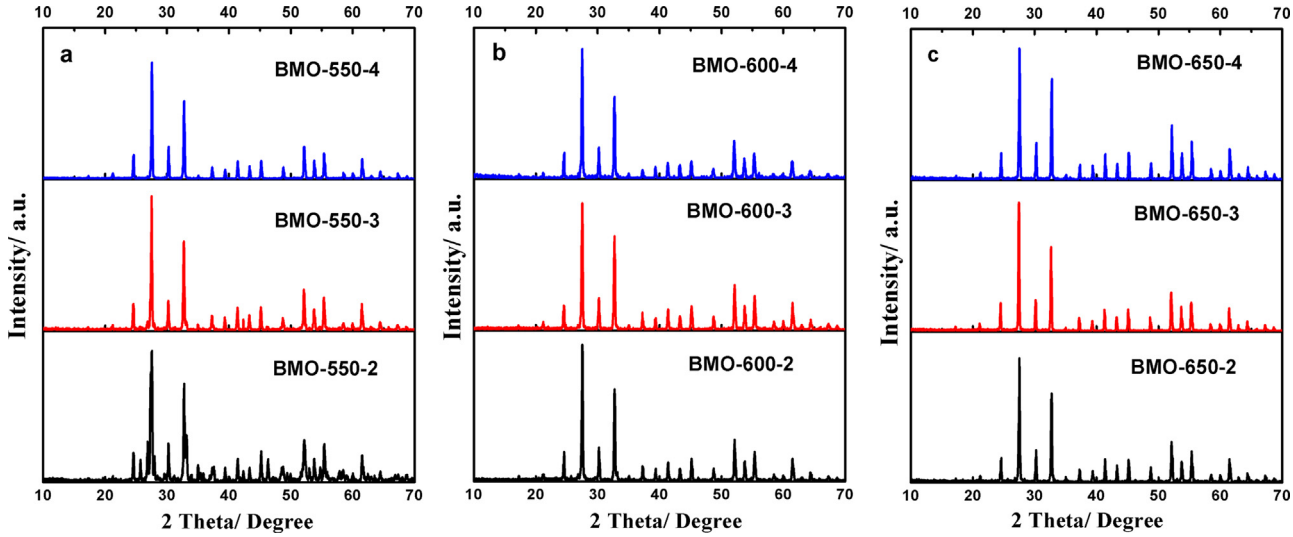

Fig. 2. XRD patterns of BMO samples calcined at 550 °C (a), 600 °C (b) and 650 °C (c) as a function of reaction time.

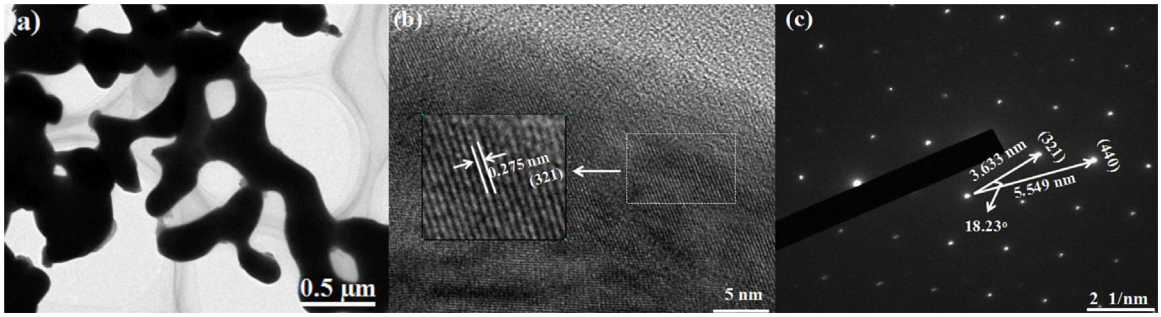

Fig. 3. TEM (a), HRTEM (b) images and SAED (c) pattern of BMO-550-4 sample.

[39,50]. The corresponding band gap was calculated by the following formula based on Fig. 5(a) [51,52]:

$$(ah\nu)^n = A(h\nu\text{-}E_g)$$

Where a, h, ν, A, E_g and n represent the absorption coefficient, Planck constant, light frequency, the proportionality constant, the band gap and 1/2 or 2 (the indirect semiconductor is equal to 1/2 and the direct semiconductor is equal to 2), respectively. In this work, $Bi_{12}MnO_{20}$ is a direct semiconductor, so the n is equal to 2. Subsequently, the calculated intrinsic band gap as inserted in Fig. 5(a) is ca. 1.86 eV. What's more interesting is that the second absorption band displays extremely high absorption capability in the range of ca.680–1300 nm, indicating that the incorporation of Mn^{4+} ions into the tetrahedral of the metastable cubic γ-Bi_2O_3 to form sillenite $Bi_{12}MnO_{20}$ has successfully achieved the expectancy that the $Bi_{12}MnO_{20}$ is strongly photoactive not only in UV and visible lights but also NIR light. This outstanding absorption is probably assigned to the splitting of Mn^{4+} 3d orbits with the hybrid of O 2p orbits and the detailed explanation will be proposed in the below photocatalytic mechanism section [44,50,53]. In this case, a new intermediate band state would be introduced into the intrinsic band gap of BMO. The electron can be excited from this intermediate band (IB) state to the conduction band (CB) of BMO, inducing light absorption from long wavelengths of visible light to NIR light, and the calculated sub-band gap as referred to Fig. 5(a) is ca. 1.07 eV. Furthermore, BMO-600-4 sample exhibited the highest light absorption capability in the range of 200–1300 nm followed by BMO-650-4 and BMO-550-4 samples. This variation is probably due to two reasons that firstly, the different roughness of sample morphology as displayed Fig. S1 would affect the reflectance of illumination light on the surface of sample. Since the BMO-600-4 particles showed the smoothest surface over BMO-650-4 and BMO-550-4 samples, it probably reflected much fewer incident lights compared with other twos. Secondly, various Mn^{4+} ions were incorporated into BMO crystal as depicted in Fig. 4(c), which probably affected the light absorption properties of samples. Besides, the photoluminescence property of BMO-550-4 sample was also demonstrated in Fig. 5(b). It is well-acknowledged that the photoluminescence of semiconductor is mainly produced by the recombination of photogenerated electrons and holes or the trapping center in the band gap. It is explicit in Fig. 5(b) that the representative BMO-550-4 sample exhibits a strong emission band maximized at ca. 475 nm, which is well consistent with the first absorption peak in Fig. 5(a), and displays a small emission peak located at ca. 740 nm, which is nicely agreement with the second absorption peak in Fig. 5(a) under the excitation wavelength of 220 nm. These phenomena further confirmed that the intrinsic band gap of BMO is corresponding to the first characteristic absorption peak, and the sub-band gap is truly existed, ascribing to the second peculiar absorption peak.

To further ascertain the existence of IB in the band gap, the total and partial DOS of BMO was calculated based on first principle DFT as presented in Fig. 6. From Fig. 6(a)–(d), it can be obviously observed that the VB of BMO is mainly contributed by the hybrid of Bi 6p and O 2p orbits, and the CB is mostly resulting from the hybrid of Bi 6p, O 2p and Mn 3d orbits. More essentially, an intermediate state really appeared in the band gap, which is dominantly made up by the hybrid of O 2p and Mn 3d split orbits. This result is nicely

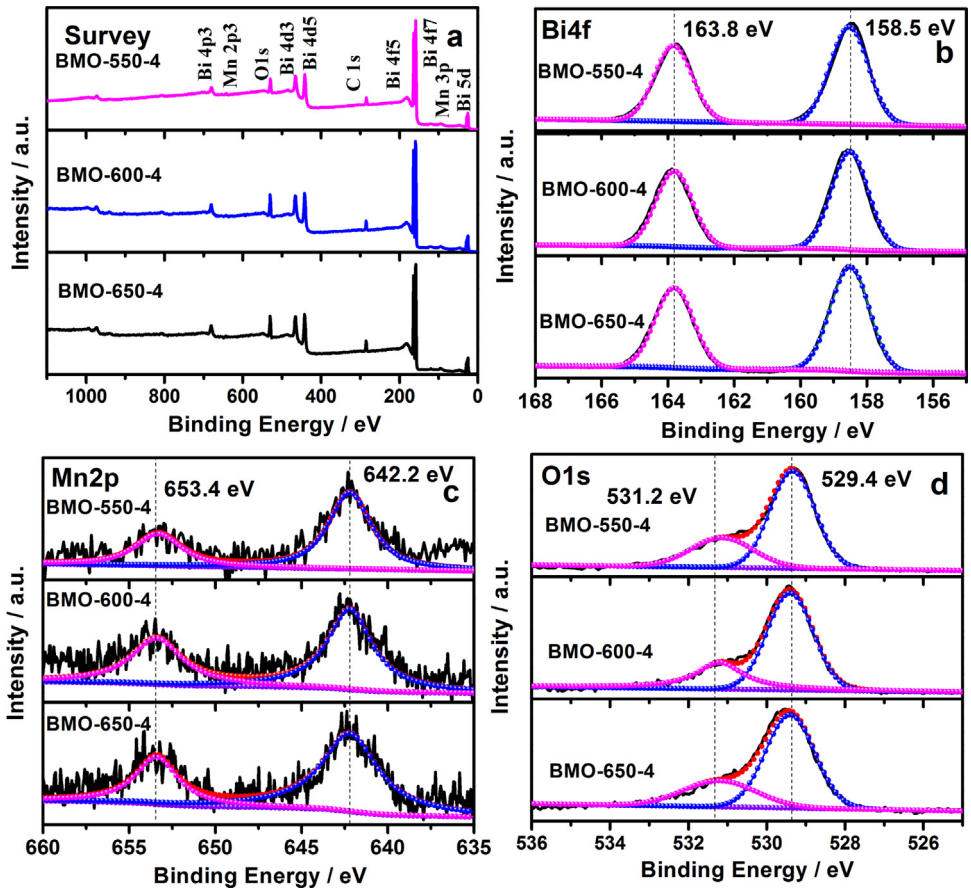

Fig. 4. XPS spectra of BMO samples: (a) survey spectrum, (b) Bi 4f spectrum, (c) Mn 2p spectrum and (d) O 1s spectrum.

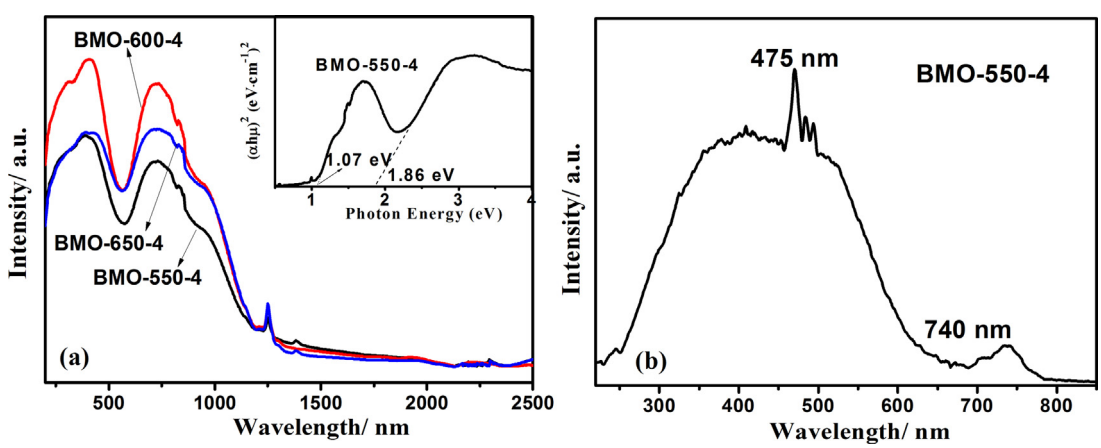

Fig. 5. DRS of BMO-550-4, BMO-600-4, BMO-650-4 (the inset is the Plots of $(\alpha h\nu)^{1/2}$ versus photon energy of BMO-550-4) (a) and photoluminescence spectrum of BMO-550-4 with the excitation wavelength of 220 nm (b).

consistent with our expectancy as described in introduction part that the electron is possible to transfer from IB to CB.

In this work, in order to investigate the full spectrum photocatalytic performance of sample under the irradiation of UV, visible and NIR lights, the photocatalytic reduction of Cr(VI) by the BMO sample was employed as target as shown in Fig. 7. Fig. 7 (a) represented the photocatalytic reduction of Cr(VI) solution by the BMO-550-4 sample under various photo-reaction conditions. It is apparent that under the irradiation of visible light but without catalyst, the concentration of Cr(VI) had no significant change, meanwhile without light irradiation but with catalyst, the concentration of Cr(VI) decreased to some extent owing to the adsorption of BMO. However, when the Cr(VI) solution was irradiated by visible light of Dy lamp in the presence of BMO particles, the concentration of Cr(VI) had been significantly reduced by 98% after 2 h light irradiation. Compared to the Cr(VI) solution in the presence of the BMO without light irradiation and the one in the absence of sample with light irradiation, the concentration of Cr(VI) solution in the presence of the BMO with light irradiation was decreased significantly, indicating that the dramatic reduction of Cr(VI) was truly resulting from photocatalysis instead of photolysis and physical adsorption. While when visible LED was employed as visible light irradiation

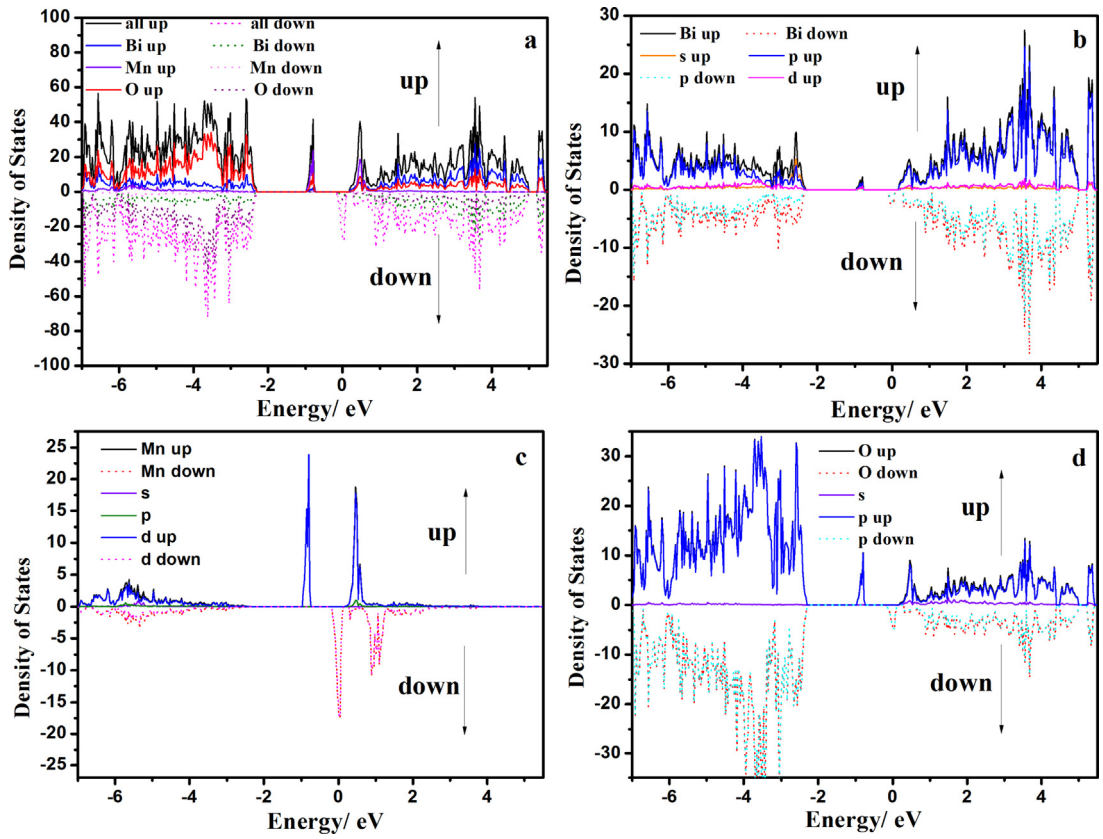

Fig. 6. The total and partial DOS projected on all (a), Bi (b), Mn (c) and O (d).

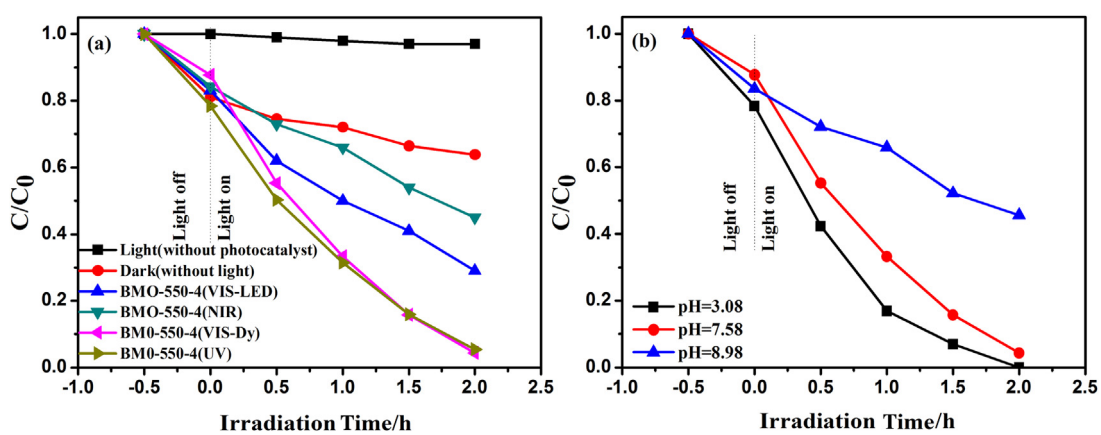

Fig. 7. The photocatalytic reduction of Cr(VI) solution over BMO-550-4 sample by various lights irradiation and different conditions (a) and the effect of pH of the Cr(VI) solution on the photocatalytic property of BMO-550-4 sample under visible light irradiation (b).

source, the photocatalytic reduction capability was decreased to 71% during 2 h, which should be due to the difference intensities of Dy lamp and 420 nm LED as presented in above experiment section. In the following, all visible light induced photocatalytic activity of samples used the Dy lamp as visible light source. When BMO sample solution was irradiated by UV light, the degradation of Cr(VI) was similar to that irradiated by visible light of Dy lamp. It is commonly known that the UV light induced photocatalytic activity should be superior over visible light driven one owing to the higher energy of UV light. Nevertheless, in this work, the total irradiation energy of UV light (20W) is much lower than that of visible light (300 W), so they presented the similar photocatalytic performance under UV and visible lights illumination. More importantly, when the BMO sample solution was irradiated by NIR light, the BMO sample still exhibited extremely outstanding Cr(VI) photocatalytic reduction property up to 50%, which should be due to the excellent photo-responsive in the range of NIR light as presented in Fig. 5(a). On the other hand, to totally remove the effect of physical absorption on the Cr (VI) photocatalytic reduction by the BMO sample, the photocatalytic reaction was also evaluated after that the Cr (VI) solution containing the BMO sample kept in dark for 3 h to reach adsorption-desorption equilibrium as supplemented in Fig. S2. The photocatalytic activity of commercial P25 was also added in this Figure. It is explicit that the BMO sample was really photocatalytic active for the Cr (VI) reduction under the irradiation of visible and NIR lights. In addition, the visible and NIR lights induced photo-catalytic activities of the BMO sample for Cr(VI) reduction were much superior over those of commercial P25. Besides, the effect

of pH value of the Cr(VI) solution on the photocatalytic reduction of Cr(VI) was also studied in Fig. 7(b). It is obvious that when the pH value was neural or acidic, the sample could present excellent photocatalytic reduction property, but much poorer for basic one. The main reason for this could be explained as follows [54,55]: at an acidic solution, Cr(VI) mainly exists as the form of $HCrO_4^-$ or $Cr_2O_7^{2-}$. In this case, the Cr(VI) is in favor of reducing to Cr(III) as listed in Eqs. (1) and (2). While at a neutral or basic circumstance, Cr(VI) will be dominantly presented as a form of CrO_4^{2-}. The corresponding reduction procedure will be the one as exhibited in Eq. (3), which is detrimental for the Cr(VI) reduction. Therefore, the photocatalyst generally shows higher Cr(VI) photocatalytic reduction activity in acidic condition but inferior one in neutral and basic conditions. From above discussion, it could be concluded that the as-synthesized BMO sample obtains a flexible reaction pH value for Cr(VI) photocatalytic reduction from acidic to neutral environment.

$$Cr_2O_7^{2-} + 14H^+ + 6e^- = 2Cr^{3+} + 7H_2O \quad (1)$$

$$HCrO_4^- + 7H^+ + 3e^- = Cr^{3+} + 4H_2O \quad (2)$$

$$CrO_4^{2-} + 4H_2O + 3e^- = Cr(OH)_3 + 5OH^- \quad (3)$$

In addition, the effect of preparation temperature, time, sample dosage and Cr(VI) concentration on the photocatalytic reduction of Cr(VI) was also investigated as appended in Fig. S3. For instance, it is obvious in Fig. S3(a) that the BMO-550-4, BMO-600-4 and BMO-650-4 samples all presented photocatalytic reduction property for Cr(VI) solution, but the BMO-550-4 sample presented the best photocatalytic followed by BMO-600-4 and BMO-650-4 samples. As we all known, the photocatalytic activity of semiconductor is mainly dependent on light absorption capability, specific surface area and crystallinity, etc. In this work, the BMO-600-4 sample exhibited the highest light absorption properties followed by BMO-650-4 and BMO-550-4 samples as displayed in Fig. 5(a). Besides, the specific surface areas of BMO-550-4, BMO-600-4 and BMO-650-4 samples are 3.5, 3.8 and 3.7 m^2/g, respectively. In addition, the crystallinity of three samples was all similar. In this case, the photocatalytic activity of the BMO-600-4 sample should theoretically higher than those of BMO-650-4 and BMO-550-4 samples. However, the experimental results were opposite. This abnormal phenomenon may be owing to the various Mn^{4+} ions incorporation in BMO crystal as determined in Fig. 4(c). The detailed research about this would be our next works. From Fig. S3, it can be obtained that the optimal condition for the photocatalytic reduction of Cr(VI) was that the BMO sample prepared at 550 °C for 4 h with the dosage of 2 g/L in the 10 mg/L of Cr(VI) solution could exhibit the best photocatalytic performance.

Besides, for the sake of confirming the reduction of Cr(VI) rather than adsorption, the Cr2p XPS analysis of the BMO-550-4 sample after photocatalytic reaction for 2 h was conducted as presented in Fig. 8. It can be clearly seen that some significant peaks appeared in the Cr2p XPS spectrum, which could be fitted into two couples of peaks. The first couple of peaks located at 579.3 and 588.4 eV could be assigned to the binding energies of Cr(VI)$2p_{3/2}$ and Cr(VI)$2p_{1/2}$, respectively; the second strong couple of peaks situated at 577.8 and 586.9 eV could be ascribed to the binding energies of Cr(III)$2p_{3/2}$ and Cr(III)$2p_{1/2}$, respectively. So the Cr2p XPS could prove that the Cr(VI) was actually reduced into Cr(III) in the presence of the BMO photocatalyst with the irradiation of light.

On the other hand, the photocatalytic activity of the BMO was also investigated by the degradation of ARG in aqueous solution under visible light irradiation as displayed in Fig. 9. As compared to those of blank one with light irradiation and the one in the absence of BMO, the BMO-550-4 sample showed relatively good ARG photodegradation property irradiated by visible light. Thus, the BMO sample not only shows excellent UV, visible, NIR lights induced

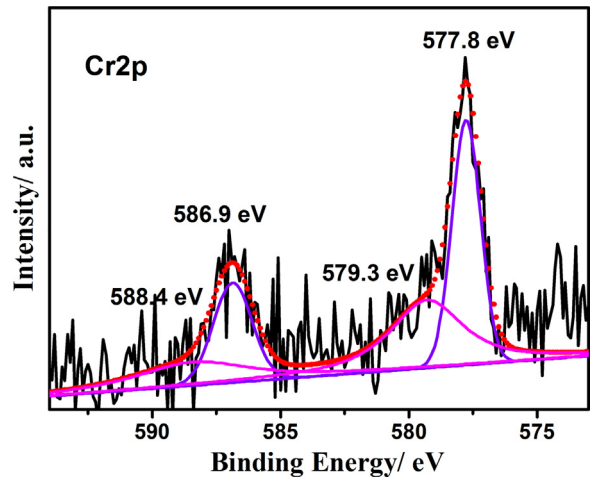

Fig. 8. XPS spectrum of Cr2p for the sample after the photoreduction of Cr(VI).

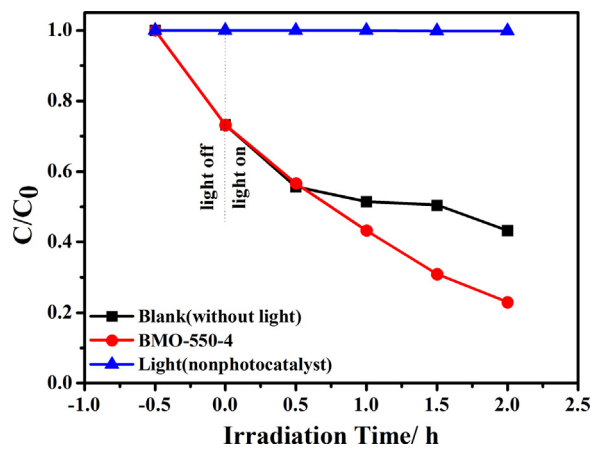

Fig. 9. Photocatalytic degradation of ARG over BMO-550-4 under various conditions.

photocatalytic reduction activity but also nice visible light driven photocatalytic oxidation property.

In order to analyze the photocatalytic mechanism of BMO clearly, the radical species trapping experiments were carried out in the photocatalytic degradation of ARG over the BMO sample under visible light irradiation as shown in Fig. 10(a). In those experiments, $Na_2C_2O_4$ (2 mM) and 1, 4-benzoquinone (BQ, 2 mM) were used as the scavengers of h^+ and $^{\bullet}O_2^-$ species in the photocatalytic process, respectively. It is distinct that in the presence of BQ scavenger, the photocatalytic degradation of ARG by the BMO was decreased to some extent; while in the presence of $Na_2C_2O_4$ scavenger, the photocatalytic activity was dramatically reduced. Meanwhile, to remove the effect of the introduction of $Na_2C_2O_4$ on the pH value of ARG solution, the pH value of ARG solution in the presence of $Na_2C_2O_4$ (pH = 5.18) was adjusted to 5.07 as the one before adding $Na_2C_2O_4$. The corresponding photocatalytic test was supplemented in Fig. S4, in which the photocatalytic activity of BMO was still significantly decreased compared with the one without tuning pH value in the presence of $Na_2C_2O_4$. So the above results indicate that the h^+ and $^{\bullet}O_2^-$ species are active for the ARG photocatalytic degradation but the h^+ species play the dominant role. In addition to h^+ and $^{\bullet}O_2^-$ species, the ·OH species is also one of the most active oxidation species. Thus, the production of ·OH species in the photodegradation of ARG over BMO sample under visible light irradiation was examined by checking the emission intensity of terephthalic acid (TA) solution containing 2×10^{-3} M NaOH and BMO particles at ca. 425 nm. This test can demonstrate

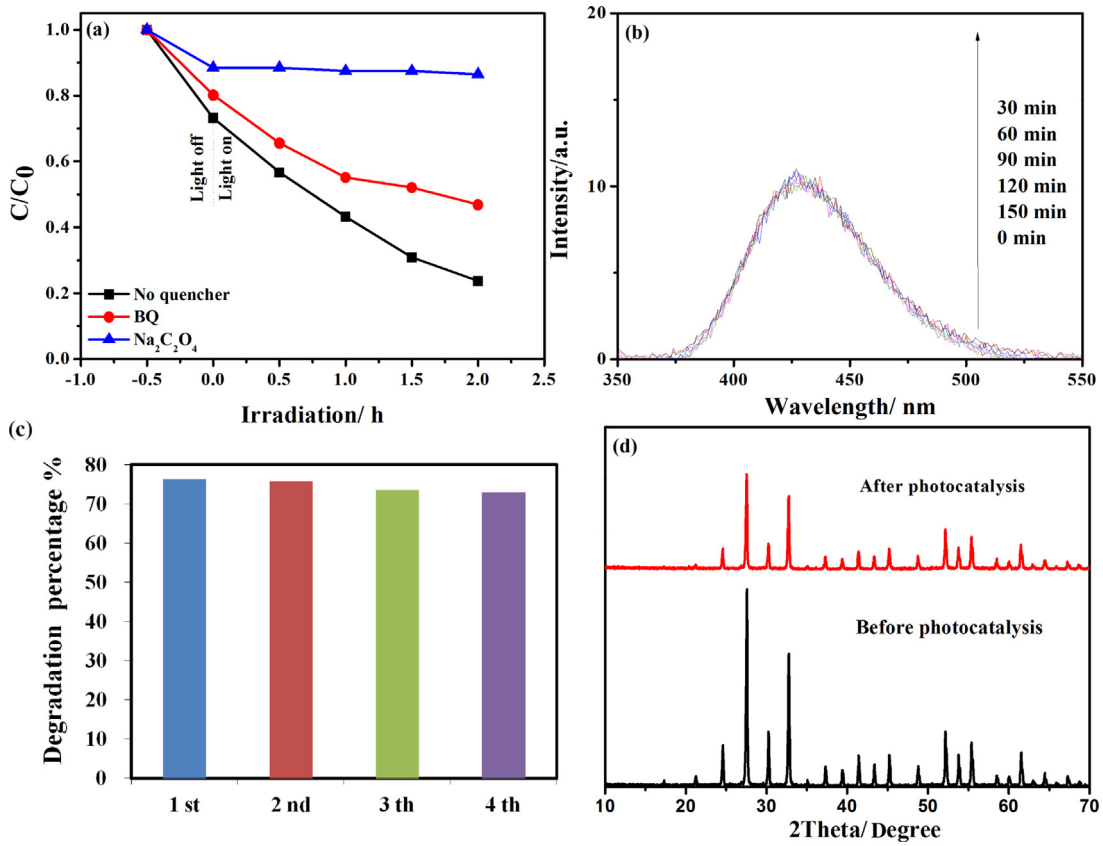

Fig. 10. The effect of various scavengers on the photodegradation of ARG solution under visible light irradiation (a), photoluminescence spectra of terephthalic acid solution containing BMO-550-4 particles after visible light irradiation with respect to irradiation time (b), photodegradation stability of BMO-550-4 sample for ARG solution (c) and XRD patterns of BMO-550-4 sample before and after photodegradation of ARG solution (d).

that the higher emission intensity of TA solution is, the more ·OH species produces in the photocatalytic process [56]. However, there is no significant variation observed in Fig. 10(b) with increasing irradiation time, implying that no dramatic amount of •OH species produced during the photocatalytic process and the reason would be depicted in the following photocatalytic mechanism section. In addition, the photocatalytic stability of the BMO sample for ARG degradation under the illumination of visible light was detected by evaluating photocatalytic recycle and XRD patterns of the BMO sample before and after photodegradation process as displayed in Fig. 10(c) and (d), respectively. It is obvious that after 4 runs of photodegradation reaction, the BMO sample still presented high ARG degradation ability with only 5% decrement; moreover, no significant change happened to the crystal structure over the XRD patterns for the BMO samples before and after photodegradation. Thereby, the as-fabricated BMO product also obtained excellent photocatalytic stability in addition to wide light responsive performance.

Finally, to explain the high photocatalytic performance of the BMO product in the full spectrum of UV, visible and NIR lights, the possible mechanism was proposed as follows. The framework of $Bi_{12}MnO_{20}$ crystal structure is constructed by the corner sharing of MnO_4 tetrahedrons and Bi-O polyhedrons as displayed in Fig. 11(a). Nine Mn^{4+} ions are situated at the body center and corner of unit cell, respectively, to form discrete MnO_4 tetrahedrons; while the Bi^{3+} ions are coordinated by seven O atoms to form a distorted BiO_7 polyhedron as demonstrated in Fig. 11(b). Firstly, Bi^{3+} ions are connected with five O atoms, the distance of which varies from 2.067 to 2.704 Å, to build the first coordination sphere. This coordination sphere presents incomplete octahedral arrangement. Meanwhile, the active Bi^{3+} $6s^2$ lone pair, opposite to the nearest O atom, will complete the distorted octahedral. The residue two O atoms will electrostatically connected to both sides of Bi^{3+} $6s^2$ lone pair with the distance of 3.063 and 3.313 Å, separately. Such peculiar structure of distorted BiO_7 polyhedron will produce a dipole moment paralleled to the Bi^{3+} $6s^2$ lone pair, which is beneficial for the separation of photogenerated hole-electron pairs, and eventually, positively contributes to the photocatalytic activity of $Bi_{12}MnO_{20}$ [57,58].

In addition to the contribution of charge carriers' separation, the band gap, the induction of intermediate band state, CB and VB positions, etc. of photocatalyst are also essential factors for the high performance of various photocatalysis. Under this consideration, the approximate VB position of BMO-550-4 was determined to be 1.4 eV, which is related to Fermi level, by UPS spectrum as showed in Fig. 12. Subsequently, the CB position of the BMO sample could be calculated as −0.46 eV based on the equation $E_{CB} = E_{VB}$-Eg and the DRS in Fig. 5(a). Besides, as described in Figs. 5 (a), (b) and 6, in addition to the intrinsic CB and VB, there should be an IB state introduced into the band gap since a strong sub-absorption peak appeared in the range of 680–1300 nm. The position of this IB was deduced to 0.61 eV referred to Fig. 5(a) and the position of CB. This sub-transition is probably owing to the splitting of Mn^{4+} 3d orbits. When the Mn^{4+} ions were incorporated into the tetrahedral sites of the metastable cubic γ-Bi_2O_3, the MnO_4 tetrahedrons would produce and the $Bi_{12}MnO_{20}$ crystal would form. In this case, the 3d orbits of Mn^{4+} in tetrahedron were prone to splitting into e_g and t_{2g} orbits. The e_g orbits would be occupied by the electrons. Then lower energy of e_g orbits entered into band gap to form IB, while higher energy of t_{2g} hybridized with CB [44,50,53,58]. So the sub-transition could be happened between IB and CB.

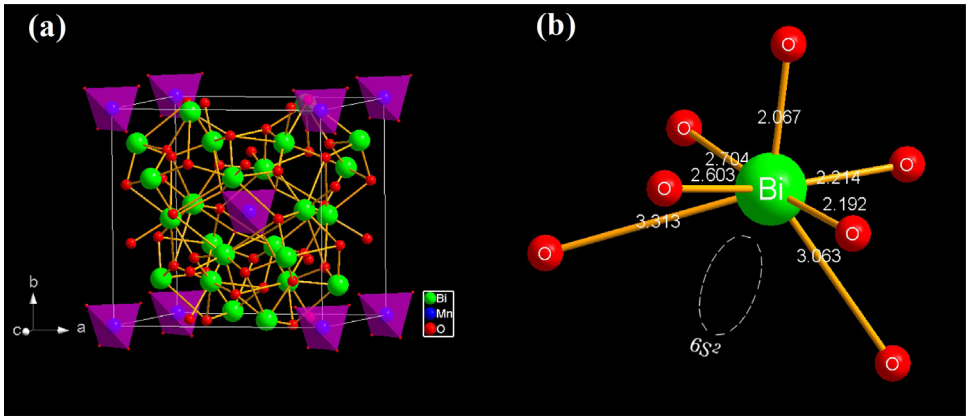

Fig. 11. Crystal structure (a) and the surrounding environment of Bi atom coordinated by seven O atoms for BMO photocatalyst.

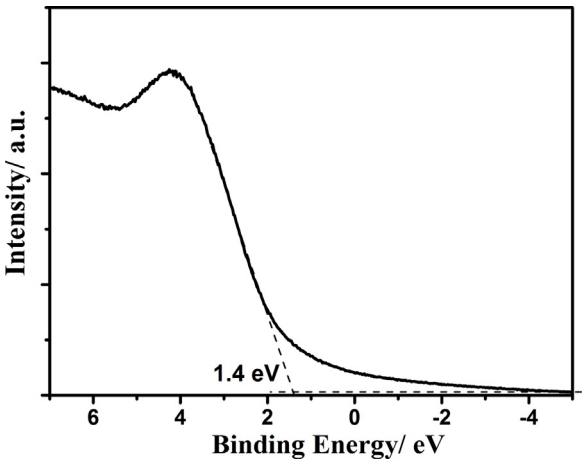

Fig. 12. UPS spectrum of BMO-550-4 for the valence band position.

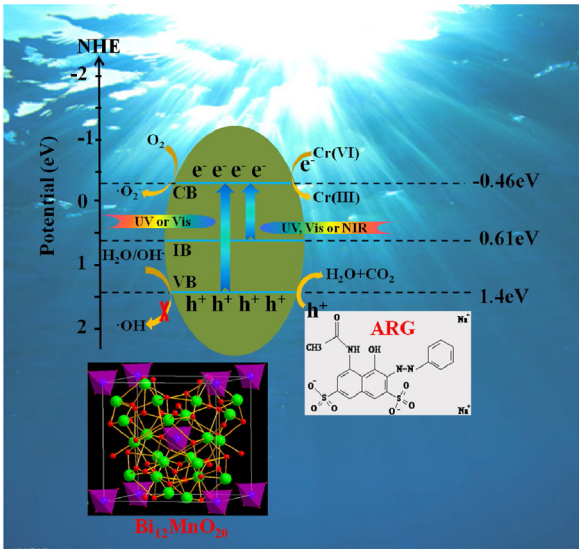

Fig. 13. Possible photocatalytic mechanism of the BMO sample.

Based on the above discussion and analysis, the possible UV, visible and NIR lights responsive photocatalytic mechanism of BMO was demonstrated in Fig. 13. When UV or visible lights irradiated the BMO, the electrons could be transferred from VB to CB, while as the BMO was illuminated by UV, visible or NIR lights, the electrons could also be moved from IB to CB. The photogenerated hole in the VB, composed by hybridization of Bi 6p and O 2p orbits, could directly oxidize the ARG; while the photogenerated electron in the CB, originated from VB and IB, could directly reduce the Cr(VI) to Cr(III) since the position of CB is higher than that of Cr(VI)/Cr(III) (+0.82 V) [59]. Meanwhile, the photo-induced electron in the CB could also react with surface absorbed O_2 to produce $^{\bullet}O_2^{-}$, finally producing oxidation activity. Besides, the photogenerated electron in the CB also possibly came from the surface absorbed ARG since the ARG could absorb visible light and then transferred the excited electron to the CB of BMO sample [60]. To further verify the possibility of ARG sensitization on the visible light induced photocatalytic activity of the BMO sample, the photocatalytic degradation of colorless tetracycline by the BMO sample under the visible light irradiation, which can eliminated the sensitization effect from contamination, was also evaluated in Fig. S5. It is apparent that the BMO sample still presented nice visible light responsive tetracycline decomposition property, indicating the BMO sample was self-active for the visible light induced photocatalysis. Therefore, the possibility of ARG sensitization on the ARG degradation by BMO was not so high, which was not drawn in Fig. 13. On the other hand, it was impossible to produce ·OH species by reacting photo-produced hole with H_2O or OH^- since the VB position of BMO is much negative as compared to that of ·OH/H_2O or OH^- (2.27 eV) [61], which is well consistent with the active species trapping experiments as presented in Fig. 10.

4. Conclusions

A novel sillenite-type $Bi_{12}MnO_{20}$ has been successfully prepared by a facile sol-gel method. The optimal synthesis conditions for $Bi_{12}MnO_{20}$ were calcined at 550 °C for 4 h. $Bi_{12}MnO_{20}$ exhibited two strong characteristic absorption bands, covering the full spectrum of UV, visible and NIR lights. The promising optical properties of $Bi_{12}MnO_{20}$ were mainly induced by the peculiar Mn^{4+} incorporation in the tetrahedral sites of $Bi_{12}MnO_{20}$ to produce intermediate band state into band gap, which was further confirmed by the DFT calculation. More importantly, under the irradiation of UV, visible and NIR lights, Cr(VI) could be significantly reduced to Cr(III) in the presence of $Bi_{12}MnO_{20}$ and the reaction environment was flexible from acid to neutral condition. Besides, the optimal Cr(VI) photocatalytic reduction conditions over $Bi_{12}MnO_{20}$ were that the BMO sample prepared at 550 °C for 4 h with the dosage of 2 g/L in the 10 mg/L of Cr(VI) solution. On the other hand, $Bi_{12}MnO_{20}$ was also active for the photocatalytic oxidation of ARG with visible light illumination and the main active species for ARG degradation were h^+ and $^{\bullet}O_2^{-}$.

Author contributions

Y. Wu and M.M. Li contributed equally to this paper. G.K. Zhang and X.Y. Wu conceived the project; M.M. Li performed the experiments; X.Y. Wu and M.M. Li wrote the paper. G.K. Zhang helped to discuss the results and the corresponding analysis.

Acknowledgments

This work was supported by the National Natural Science Foundation of China (NSFC No. 51472194 and No. 51602237), the National Basic Research Program of China (973 Program No.2013CB632402), the Natural Science Foundation of Hubei Province (2016CFA078) and the Fundamental Research Funds for the Central Universities (WUT:2017 IVA 039).

Appendix A. Supplementary data

Supplementary data associated with this article can be found, in the online version, at 10.1016/j.apcatb.2017.07.025.

References

[1] L.D. Zhang, M. Fang, Nano Today 5 (2010) 128–142.
[2] P. Verma, Y. Kuwahara, K. Mori, H. Yamashita, J. Mater. Chem. A 4 (2016) 10142–10150.
[3] Z. Sun, T. Liao, L. Kou, Sci. China Mater. 60 (2017) 1–24.
[4] J. Liu, D.F. Xue, Adv. Mater. 20 (2008) 2622–2627.
[5] B. Cao, G.S. Li, H.X. Li, Appl. Catal. B: Environ. 194 (2016) 42–49.
[6] J.J. Testa, M.A. Grela, M.I. Litter, Environ. Sci. Technol. 38 (2004) 1589–1594.
[7] Y. Li, W.Q. Cui, L. Liu, R.L. Zong, W.Q. Yao, Y.H. Liang, Y.F. Zhu, Appl. Catal. B: Environ. 199 (2016) 412–423.
[8] M.V. Dozzi, A. Saccomanni, E. Selli, J. Hazard. Mater. 211–212 (2012) 188–195.
[9] K. Tanaka, K. Padermpole, T. Hisanaga, Water Res. 34 (2000) 327–333.
[10] L. Yang, Y. Xiao, S. Liu, Y. Li, Q. Cai, S. Luo, G. Zeng, Appl. Catal. B: Environ. 94 (2010) 142–149.
[11] M. Costa, Toxicol. Appl. Pharm. 188 (2003) 1–5.
[12] D. Park, Y.S. Yun, J.M. Park, J. Colloid Interface Sci. 317 (2008) 54–61.
[13] P. Mohapatra, S. Samantaray, K.M. Parida, J. Photochem. Photobiol. A: Chem. 170 (2005) 189–194.
[14] K.H. Cheung, J.D. Gu, Int. Biodeterior. Biodegrad. 59 (2007) 8–15.
[15] H.B. Yu, S. Chen, X. Quan, H.M. Zhao, Y.B. Zhang, Environ. Sci. Technol. 42 (2008) 3791–3796.
[16] D.D. Tang, G.K. Zhang, Ultrason. Sonochem. 37 (2017) 208–215.
[17] X.D. Meng, G.K. Zhang, N. Li, Chem. Eng. J. 314 (2017) 249–256.
[18] Z. Sun, T. Liao, L. Sheng, L. Kou, J.H. Kim, S.X. Dou, Chem. A Eur. J. 22 (2016) 11357–11364.
[19] L. Zhang, Q.H. Zhang, H.Y. Xie, J. Guo, H.L. Lyu, Y.G. Li, Z.G. Sun, H.Z. Wang, Z.H. Guo, Appl. Catal. B: Environ. 201 (2017) 470–478.
[20] J. Liu, F. Liu, K. Gao, J.S. Wu, D.F. Xue, J. Mater. Chem. 19 (2009) 6073–6084.
[21] P.F. Fu, P.Y. Zhang, Appl. Catal. B: Environ. 96 (2010) 176–184.
[22] Y. Li, W.Q. Cui, L. Liu, R.L. Zong, W.Q. Yao, Y.H. Liang, Y.F. Zhu, Appl. Catal. B: Environ. 199 (2016) 412–423.
[23] S. Weon, W. Choi, Environ. Sci. Tehnol. 50 (2016) 2556–2563.
[24] Y.C. Zhang, J. Li, M. Zhang, D.D. Dionysiou, Environ. Sci. Technol. 45 (2011) 9324–9331.
[25] X.F. Hu, H.H. Ji, F. Chang, Y.M. Luo, Catal. Today 224 (2014) 34–40.
[26] H. Chu, X. Liu, B. Liu, G. Zhu, W. Lei, H. Du, J. Liu, J. Li, C. Li, C. Sun, Sci. Rep. 6 (2016) 35304.
[27] X.Y. Wu, J.T. Wang, G.K. Zhang, K. Katsumata, K. Yanagisawa, T. Sato, S. Yin, Appl. Catal. B: Environ. 201 (2017) 128–136.
[28] N. Wei, H.Z. Cui, Q. Song, L.Q. Zhang, X.J. Song, K. Wang, Y.F. Zhang, J. Li, J. Wen, J. Tian, Appl. Catal. B: Environ. 198 (2016) 83–90.
[29] J. Tian, Y.H. Sang, G.W. Yu, H.D. Jiang, X.N. Mu, H. Liu, Adv. Mater. 25 (2013) 5075–5080.
[30] W.P. Qin, D.S. Zhang, D. Zhao, L.L. Wang, K.Z. Zheng, Chem. Commun. 46 (2010) 2304–2306.
[31] Y.H. Sang, Z.H. Zhao, M.W. Zhao, P. Hao, Y.H. Leng, H. Liu, Adv. Mater. 27 (2015) 363–369.
[32] G. Wang, B.B. Huang, X.C. Ma, Z.Y. Wang, X.Y. Qin, X.Y. Zhang, Y. Dai, M.H. Whangbo, Angew. Chem. Int. Ed. 52 (2013) 4810–4813.
[33] H. Li, J. Shang, H.J. Zhu, Z.P. Yang, Z.H. Ai, L.Z. Zhang, ACS Catal. 6 (2016) 8276–8285.
[34] X. Ding, W.K. Ho, J. Shang, L.Z. Zhang, Appl. Catal. B: Environ. 182 (2016) 316–325.
[35] X.F. Chang, G. Yu, J. Huang, Z. Li, S.F. Zhu, P.F. Yu, C. Cheng, S.B. Deng, G.B. Ji, Catal. Today 153 (2010) 193–199.
[36] H.L. Tan, X.M. Wen, R. Amai, Y.H. Ng, J. Phys. Chem. Lett. 7 (2016) 1400–1405.
[37] Y.Y. Zhu, Y.J. Wang, Q. Ling, Y.F. Zhu, Appl. Catal. B: Environ. 200 (2017) 222–229.
[38] G.K. Dinesh, S. Anandan, T. Sivasankar, Environ. Sci. Pollut. Res. 23 (2016) 20100–20110.
[39] W.F. Yao, H. Wang, X.H. Xu, X.F. Cheng, J. Huang, S.X. Shang, X.N. Yang, M. Wang, Appl. Catal. A: Gen. 243 (2003) 185–190.
[40] Q.F. Han, J. Zhang, X. Wang, J.W. Zhu, J. Mater. Chem. A 3 (2015) 7413–7421.
[41] Z. Wan, G.K. Zhang, Sci. Rep. 4 (2014) 6298.
[42] Q.R. Deng, X.H. Xia, M.L. Guo, Y. Gao, G. Shao, Mater. Lett. 65 (2011) 2051–2054.
[43] G.S. Shao, J. Phys. Chem. C 113 (2009) 6800–6808.
[44] Y.T. Meng, H.C. Genuino, C.H. Kuo, H. Huang, S.Y. Chen, L.C. Zhang, A. Rossi, S.L. Suib, J. Am. Chem. Soc. 135 (2013) 8594–8605.
[45] M.A. Kostowskyj, D.W. Kirk, S.J. Thorpe, Int. J. Hydrogen Energy 35 (2010) 5666–5672.
[46] Z. Wan, G.K. Zhang, X.Y. Wu, S. Yin, Appl. Catal. B: Environ. 207 (2017) 17–26.
[47] L. Jin, L.P. Xu, C. Morein, C.H. Chen, M. Lai, S. Dharmarathna, A. Dobley, S.L. Suib, Adv. Funct. Mater. 20 (2010) 3373–3382.
[48] X.Y. Wu, S. Yin, B. Liu, M. Kobayashi, M. Kakihana, T. Sato, J. Mater. Chem. A 2 (2014) 20832–20840.
[49] X.Y. Wu, K.K. Zhang, G.K. Zhang, S. Yin, Chem. Eng. J. 325 (2017) 59–70.
[50] Y.G. Wang, R. He, M. Yang, T. Wen, H. Zhang, J. Liang, Z.S. Lin, Y.X. Wang, G.B. Li, J.H. Lin, CrystEngComm 14 (2012) 1063–1068.
[51] Y. Zhou, Q.Y. Yi, M.Y. Xing, L. Shang, T.R. Zhang, J.L. Zhang, Chem. Commun. 52 (2016) 1689–1692.
[52] K. Peng, L.J. Fu, H.M. Yang, J. Ouyang, Sci. Rep. 6 (2016) 19723.
[53] Q.R. Deng, X.H. Xia, M.L. Guo, Y. Gao, G. Shao, Mater. Lett. 65 (2011) 2051–2054.
[54] H. Wang, X.Z. Yuan, Y. Wu, G.M. Zeng, X.H. Chen, L.J. Leng, Z.B. Wu, L.B. Jiang, H. Li, J. Hazard. Mater. 286 (2015) 187–194.
[55] E. Petala, M. Baikousi, M.A. Karakassides, G. Zoppellaro, J. Filip, J. Tucek, K.C. Vasilopoulos, J. Pechousek, R. Zboril, Phys. Chem. Chem. Phys. 18 (2016) 10637–10646.
[56] S.F. Chen, X.L. Yu, H.Y. Zhang, W. Liu, J. Electrochem. Soc. 157 (2010) K96–K102.
[57] X.P. Lin, F.Q. Huang, W.D. Wang, Y.J. Xia, Y.M. Wang, M.L. Liu, J.L. Shi, Catal. Commun. 9 (2008) 572–576.
[58] X.B. Qiao, Y.F. Pu, Y.Z. Li, Y.L. Huang, H. Cheng, H.J. Seo, Powder Tech. 287 (2016) 277–284.
[59] K. Vignesh, R. Priyanka, M. Rajarajan, A. Suganthi, Mater. Sci. Eng. B 178 (2013) 149–157.
[60] B. Cao, G.S. Li, H.X. Li, Appl. Catal. B: Environ. 194 (2017) 42–49.
[61] H.W. Huang, Y. He, X.W. Li, M. Li, C. Zeng, F. Dong, X. Du, T.R. Zhang, Y.H. Zhang, J. Mater. Chem. A 3 (2015) 24547–24556.